

Vorticity and Wave Motion in a Compressible Protoplanetary Disk

S. S. Davis

NASA Ames Research Center, MS 260-1, Moffett Field CA, 94035

650-604-4197, sdavis@mail.arc.nasa.gov

July 11, 2001

Abstract

The impact of an isolated vortex in a compressible Keplerian disk is examined using higher order numerical solutions of the Euler and entropy-conserving Energy equations. The vortex is stretched by the background shear flow with longer lasting anticyclonic vortices persisting for about 10 vortex revolutions. Simultaneously, the vortex emits transient radial waves consisting mainly of axisymmetrical weak shock waves and a slower, nonaxisymmetric Rossby wave. These waves may contribute to certain transient events in protoplanetary disks. The vortex stretching and waves were found to have little long-term feedback on the baseline “standard solar nebula” disk structure and confirm the extremely stable structure of non self-gravitating disks.

I Introduction

Light, cool disks with approximately Keplerian rotation curves are common models for protoplanetary disks. Such gaseous disks form the background for solid body accretion and gas dynamic processes that no doubt plays a critical role in the planet formation process (Weidenschilling & Cuzzi 1993, Beckwith et al. 2000). Earlier work on idealized infinitely thin disks (Lynden-Bell & Pringle 1974, Adams et al. 1989) has evolved to investigations of multi dimensional disks with vertical and radial mean flow structure. (Klahr et al. 1999) There is now an extensive literature base concerning the dynamical properties of such disks. Furthermore, a number of disk-related wave systems were identified as being relevant to the solar nebula. A survey of the field to the mid 1990s by Papaloizou & Lin 1995 emphasizes the role of the underlying gas and seriously consider wave motion as one option for mass and momentum transfer.

The strong synergy between geophysical and astrophysical problems was recognized decades ago. In particular, coherent vortices as an important flow structure in protostellar disks was advocated by v. Weizacker 1945 and examined in some detail by Adams & Watkins 1995. Bracco et al. 1998, 1999 consider transport properties of vortices in barotropic fluids using spectral-based finite-difference techniques with direct application to protoplanetary disks. They showed that coherent vortices last long enough to form “lumpy structures” that may concentrate solid objects and accelerate planetesimal formation. Recently, Godon & Livio 1999 extended the work to a compressible viscous nebula by simulating discrete vortices in a viscous accretion disk using related pseudo-spectral numerical methods. Using a polytropic gas model they find that anticyclonic vortices last from 10 to 100 revolutions depending on the chosen viscosity. No acoustic or shock wave motion is reported, but their equations clearly support such waves. Barge & Sommeria 1995 investigate long-lived vortices in a disk and predict that particles may migrate to the center of a vortex after a few vortex revolutions so the issue of vortex dynamics in the particle accumulation process is of current interest. This paper will consider vortices in gaseous disks and the dual role of the underlying disk medium in propagating a variety of wave systems throughout the disk and in simultaneously stretching the vortex by localized velocity shear.

Sheehan et al 1999 examine the analogy between meteorological and cosmological wave motions in some detail, emphasizing the role of Rossby waves. They argue that vortices and Rossby waves probably play a role in the protoplanetary nebula. Davis et al 2000 (hereafter DSC) further investigate the role of vortices and Rossby waves in a model solar nebula. They consider the evolution of a compact region of coherent vorticity using an incompressible flow model and the vorticity transport equations. They found that compact vortices induce weak Rossby waves that slowly radiate over the entire disk. The vortices ultimately dissipate, but anticyclonic vortices were shown to be more persistent than cyclonic vortices.

In this paper we expand the analysis of vortices to compressible disks and show how a vortex, once formed, can generate disturbances that propagate to the outer reaches of the disk. We use a standard model of the solar nebula with a variable thickness and power-law radial variations of the equilibrium variables. We show that discrete vortices evolve in two directions: first into a ring structure at the radial location of the vortex and second into two separate wave packets. One is a fast wave based on the acoustic time scale and the second a slower Rossby wave motion. The fast wave evolves into a weak cylindrical shock that envelops the entire disk. We find that no instability mechanisms are activated and the waves have little impact on the underlying disk structure once they traverse the disk.

A third order in space/ fourth order in time explicit numerical algorithm is developed to solve the "column averaged" Euler and Energy equations. The equations are cast in a semi-conservative form designed to exploit the underlying eigenvalue structure. The base flow assumes mechanical equilibrium with assumed density, pressure, and local disk height based on standard solar nebula models. A seeded compact vortex is chosen whose circulation is approximately the rotation rate of Jupiter and diameter appropriate for the thin disk approximation.

With respect to the question of vortex generation in a protostellar disk Li et al 2000 derive dispersion relations for unstable Rossby wave phenomena induced by a strong local entropy (temperature) gradient. Li et al. 2001 simulates this instability and subsequent anticyclonic vortex formation using numerical solutions of the Euler and energy equations. The standard solar nebula model used in this paper does not include mean variations in entropy and, as a result, only globally stable wave systems were found.

In section II the numerical problem is formulated based on a thin disk flow model that is initially in mechanical equilibrium. A new derivation of the three-dimensional equilibrium flow and the definition of the column-averaged quantities are presented in an Appendix. A semi-conservative form of the Euler and Energy equations is described and used to develop a high-resolution flux-biased finite difference algorithm. In Section III the vortex evolution is examined using instantaneous and azimuthally averaged flow quantities. Finally, the relevance of this model to some open questions regarding disk evolution is discussed.

II Problem Formulation

(a) The equilibrium flow

The equilibrium surface density and pressure from given distributions on the central-plane are derived in the Appendix. These column-averaged thermodynamic quantities define a fictitious polytrope (Hunter, 1972) that is related to the physical gas by the parameters in Table A1. The temperature of the disk is conveniently defined from the column-averaged perfect-gas equation of state in terms of the column pressure P and the surface density σ : $P/P_0 = (\sigma T)/(\sigma_0 T_0)$. The initial central-plane thermodynamic quantities ρ_0 , T_0 , n and γ are all given constants. Here we will take values representative of a "standard solar nebula." Let r_0 be 1 AU and $n = -3$ as recommended by Weidenschilling 1977. Cuzzi, et al, 1993 used $\rho_0 = 1.4 \times 10^{-9}$ g/cm³ and $T_0 = 280$ K at $r_0 = 1$. From the perfect gas equation of state (assuming a molecular weight of 2.34 g/mole), $p_0 = 13.83$ dynes/cm². The specific heat ratio γ is taken as 1.5 and the value of GM appropriate for the solar nebula.

It is useful compute the dependent variables in astronomical units as the compressible flow equations contain a number of thermodynamic quantities that are not conveniently nondimensionalized. In addition, the key role played by the sound speed is expressed in a more physical context. Length, mass, and time are taken as AU, solar mass (SM), and years (yr). Certain parameters become extremely simple in this system. For example, $G = 4\pi^2$ and $M = 1$. Table 1 indicates the major equilibrium flow parameters at several radial locations using the data in the Appendix.

TABLE 1
Equilibrium Flow Parameters

r, AU	H, AU	σ , SM/AU ²	P, SM/yr ²	T, K	a, AU/yr
1	0.082	2.05E-04	7.73E-06	180	0.274
5	0.409	4.11E-05	3.09E-07	36	0.123
10	0.817	2.05E-05	7.73E-08	18	0.087
15	1.226	1.37E-05	3.44E-08	12	0.071
20	1.634	1.03E-05	1.93E-08	9	0.061

The second column is the half height of the nebula using formulas in the Appendix. The computed wave motions should have wavelengths larger than these values to avoid three-dimensional effects. The surface density, pressure, and temperature decrease quite rapidly. The last column is the local sound speed which decays in this particular case as $r^{-1/2}$; the same decay rate as the basic Keplerian flow so the azimuthal Mach number stays constant at about 23. The entropy is conveniently measured by the polytropic "constant" $K' = P \sigma^{-\Gamma}$. It is initially a global constant of about 183 in astronomical units. The ratio of gravitational (GM/r) to thermal (P/ σ) energy, which governs the disk thickness, is also constant and approximately equal to 1050.

(b) Equations of motion and solution method

The equations of motion can be written in a variety of ways. Analytically based asymptotic methods were very popular in the 1950s and 60s and used conventional non-conservative equation sets. In the continuing search for effective numerical methods, the conservative form of the equations seems preferable. Unfortunately, astrophysical problems include gravitational body-force terms that upset the symmetry of the classical conservation equations. In addition, when expressed in non-Cartesian coordinates the fully conservative equations become quite complex. Davis 2001 compares straightforward use of the classical conservation equations in curvilinear coordinates and showed that the effect of rotation could be significant. The numerical error when computing a simple Keplerian flow in polar coordinates was examined and traced to an incompatible finite-differencing sequence.

The alternate form of the Euler/Energy equation is shown below. It is based on the fact that astrophysical flow fields are driven by differences between two large quantities (gravitational and centrifugal forces). If these relatively large quantities can be expressed as source terms, incompatible discretization errors will not occur. If u_r and u_θ are polar velocities, e_t the total energy, p the pressure, and ρ the density, then

$$\frac{\partial}{\partial t} \begin{bmatrix} r\rho \\ r\rho u_\theta \\ r\rho u_r \\ re_t \end{bmatrix} + \frac{\partial}{\partial \theta} \begin{bmatrix} \rho u_\theta \\ p + \rho u_\theta^2 \\ \rho u_\theta u_r \\ (e_t + p)u_\theta \end{bmatrix} + \frac{\partial}{\partial r} \begin{bmatrix} r\rho u_r \\ r\rho u_\theta u_r \\ r(p + \rho u_r^2) \\ r(e_t + p)u_r \end{bmatrix} + \begin{bmatrix} 0 \\ \rho u_\theta u_r \\ -p - \rho u_\theta^2 + \rho \frac{GM}{r} \\ \rho \frac{GM}{r} u_r \end{bmatrix} = 0 \quad (1)$$

where the dependent variable $Q = [\rho, \rho u_\theta, \rho u_r, e_t]$ and the second and third vectors are fluxes. This equation has two important properties. First, a baseline Keplerian flow is satisfied exactly by the undifferentiated source terms. Second, the (r, θ) eigenvalues can be shown to be $[u_r, u_r, u_r+c, u_r-c]$ and $[u_\theta, u_\theta, u_\theta+c, u_\theta-c]$ where c is the local sound speed. This makes it easier to construct wave-following algorithms in direct analogy with Cartesian systems. The physical nature of the solar nebula is such that perturbation radial velocities are close to sonic while the baseline azimuthal velocity is at quite a high Mach number ($u_\theta/c \sim 20$). This form of the Euler equations has been presented previously (Mair et al 1988; Godon 1997) but the favorable properties mentioned above seem not to have been utilized.

The equations are integrated in time using an explicit numerical algorithm. Higher order methods are necessary when computing evolving waves on reasonably sized grids. A critical feature is the need to transmit waves with minimal phase error (dispersion). The change in Q over a small time increment is computed using a fourth-order Runge-Kutta method. Spatial derivatives are computed with a third-order biased upwind scheme (a five-point stencil with three upwind and one downwind mesh point). The spatial stencil was applied to a flux-split form of eq (1). The two flux vectors can each be decomposed into the product of a 4×4 "Jacobian matrix" and the vector of dependent variables Q . The Jacobian matrix, in turn, can be converted by a similarity transformation into a product of three 4×4 matrices consisting of a pre-matrix, a diagonal matrix, and a post-matrix. The elements of the diagonal matrix corresponding to θ and r are

$[u_\theta, u_\theta, u_\theta + c, u_\theta - c]$ and $[u_r, u_r, u_r + c, u_r - c]$ respectively. These are the allowable propagation speeds of the waves at each point in space-time. In the former case u_θ will dominate c since the azimuthal flow is highly supersonic. The radial velocities are approximately sonic so they will be more sensitive to the ambient sound speed. The sign of each of these speeds is examined and those of like sign are combined in each coordinate direction. The matrices are then recombined into two flux vectors that reduces to the matrix equation:

$$r \frac{\partial}{\partial t} Q + \frac{\partial}{\partial \theta^+} F^+ + \frac{\partial}{\partial \theta^-} F^- + \frac{\partial}{\partial r^+} G^+ + \frac{\partial}{\partial r^-} G^- + R = 0$$

where derivatives with superscript + (-) are backward (forward) biased. The most computationally extensive part of the algorithm is computing the flux vectors which is required at each stage of the Runge-Kutta time advancement algorithm (four times per time step for each coordinate direction). This finite difference scheme is contrasted with other conservation-law-based schemes aimed at precise shock wave resolution. They are usually not of high-order accuracy away from shock waves which is the trade-off for highly resolved shock waves. The development of higher order algorithms with precise shock resolution is the subject of intense current research.

Appropriate boundary conditions for this class of problems is formidable. These highly sheared flows propagate waves whose wavelength is comparable with the shear rate and commonly used radiation boundary conditions are not applicable. Considering the lack of reliable and robust numerical radiation boundary conditions, a second order boundary extrapolation was used. This simple approach was appropriate for this problem. Wave reflection from the inner boundary was not a problem. (However, disturbances seem to focus on the boundary, which is probably a numerical artifact.). The outer boundary was taken far enough away so that reflections did not yet interfere with the outwardly moving wave. Periodic boundary conditions were imposed in the azimuthal direction.

Mechanical equilibrium was disturbed by a vortex placed at 4 AU. Vortex parameters were chosen to satisfy the thin disk approximation. The vortex is distorted by the local equilibrium flow and simultaneously transforms some of its energy into an outwardly propagating trailing spiral. The computational domain consists of a disk ranging from 1 to 24 AU using $(\theta, r) = (65, 300)$ mesh points. Additional computations were made on $(125, 300)$ and $(65, 600)$ point grids with no significant changes to the flow. Both cyclonic and anticyclonic vortices were used as initial flow perturbations.

III Analysis of Vortex-induced Waves

The imposed vortex is a transient event and induces an excess velocity field upon the slightly modified mean Keplerian flow of eq (A5). This excess flow is shown in Figure 1 along with the initial patch of vorticity (maximum value about -1.0 yr^{-1}) in the third quadrant. Its core diameter is about 1 AU and peak azimuthal velocity of about .14 AU/yr. This corresponds to a circulation ($\Gamma = 2\pi r_{\text{vort}} V_{\theta \text{vort}}$) about 50 times that of Jupiter which represents a relatively strong event in the

protoplanetary nebula. The local sound speed, and disk thickness at this radius are about 3.14 AU/yr and 0.3 AU respectively. The vorticity is quite compact, but note the large extent of the vortex-induced flow including significant radial velocities. The vortex imposes a thermodynamic (pressure, density, and temperature) response on the disk. The entropy ($s = P \sigma^{-\Gamma}$) is initially constant everywhere except for a small region near the vortex. Subsequently, the flow evolves by redistributing the initial circular vortex into a sheared vorticity patch and a variety of propagating waves. Unlike the incompressible disk considered by DSC, the compressible disk supports a much more varied and complex flow structure.

Early (a few vortex revolutions) and later (many vortex revolutions) flow fields are expected to be associated with different physical effects. The former event is a relatively rapid relaxation and redistribution of the vortex caused by the dominating Keplerian shear at 4 AU. Wave radiation processes are expected to dominate later. A very important parameter relating to wave systems is the smaller flow-induced radial velocity. In the remainder of the paper we will consider both effects. These flow events are illustrated using contour diagrams and instantaneous flow patterns in sec III(a) and with azimuthally averaged quantities in sec III(b).

(a) Instantaneous Flow Patterns

Figure 2 compares perturbed vorticity contours (scaled on the instantaneous peak vorticity) for cyclonic (initial vorticity aligned with the Keplerian vorticity) and anticyclonic vorticity. The horizontal scale represents angular position ($0 < \theta < 360$) and the vertical scale is the physical radius ($3 < r, \text{AU} < 10$). The first panel in each part of Figure 2 corresponds to the vortex in Figure 1. The cyclonic vortex in Figure 2(a) shears away quite rapidly (note contours at the radius of the initial vortex) and simultaneously emits a vorticity wave that propagates radially at the local sound speed. This axisymmetric wave is still in the field of view at 8 revs but by 12 revs it has moved beyond 10 AU. The initial vortex has almost completely dissipated by 12 revs. In contrast, the anticyclonic vortex maintains its coherence for a much longer time span (Figure 12(b)). The vortex is still coherent, but it also emits a vorticity wave into the outer disk. The contours in Figure 2 are drawn relative to the peak vorticity at each time (much larger in the latter case) so the propagating waves are actually of comparable amplitudes to those in part (a). This is clarified in Figure 3 with instantaneous radial vorticity profiles at 4 revs. The peak anticyclonic vorticity is larger than the cyclonic vorticity. The propagating waves, on the other hand, have similar amplitudes. These results show that the compressible disk responds in two ways; first a local flow subject to intense velocity and secondly a wave field that is relatively insensitive to source details.

Compressible and incompressible simulations are compared in Figure 4. Part (a) shows contour maps for an anticyclonic incompressible vortex from DSC with similar characteristics to that of Figure 2(b). The same contour lines are used and the stretched vorticity near the source relative to the compressible flow is apparent. (The incompressible Rossby waves studied in DSC are very low level and do not appear with this choice of contours.) Even after 4 revolutions the incompressible vortex has stretched well beyond that of its compressible counterpart indicating that vortices in compressible flows retain coherence for longer times. The difference between the extended vorticity fields in incompressible and compressible flow can be explained by the fact

that vorticity is not a conserved quantity in the latter case. However, the potential vorticity (called generalized vortensity by Adams & Watkins 1995), defined by the ratio of vorticity to surface density is a conserved quantity. Figure 4(b) shows contours of the compressible potential vorticity using the same progression of contour values. It is much more compact and is a closer analog to the incompressible vorticity. The role of potential vorticity in particle accumulation in the protoplanetary nebula is a subject for future study.

The evolution of the wave radiation processes is shown in the following figures. Figure 5 shows vorticity and surface density contours superimposed on perturbed velocity vector after 1.33 revolutions. The perturbation vorticity has stretched significantly from its initial value and is now in the fourth quadrant in part (a) of the figure. During this early phase the flow is rapidly and continuously sheared by the baseline Keplerian flow. A positive induced radial velocity (note the velocity vectors on the outermost spiral) indicates an outward moving wave. The trailing spiral moves clockwise and outward under the influence of the baseline Keplerian flow and the induced velocities. The leading edge of the spiral is in the first quadrant at this instant. A coherent overdensity (which grew from an initially insignificant value) is visible in part (b) at the same location as the vorticity. At the same time, there is a strong density wave forming in the second and third quadrant. This strong density wave is the result of nonlinear distortion of the transient pressure and is the first indication of shock wave formation.

Readjustment of the density wave from an isolated disturbance to an axisymmetric shock wave is shown in the density contours of Figure 6. The sequence illustrates the tendency of a supersonic Keplerian shear flow to "circularize" isolated disturbances. The flow evolves as a system of trailing spirals that move very rapidly in the azimuthal direction (close to Keplerian speed, above Mach 20) and with a radial speed close to the local sound speed (Mach 1). The outermost spiral is a precursor compression wave (light spirals in the outer disk) followed by a pair of shock waves. The precursor evolves radially near the local sound speed, but the shock wave moves faster since it is continuously overtaking slower moving material. Beyond the shock wave the low level precursor wave is starting to be reflected by the imposed boundary conditions at 24 AU. Behind the shock wave is a slower wave system with a nonsymmetrical amplitude distribution. This wave system is identified as a Rossby wave based on its similarity (generation time and radial wave speed) with those computed in DSC. Of these three waves, the main disturbance is confined to the pair of shock waves steadily moving outward. By 12 revolutions the wave system has enveloped almost the whole disk. A perspective view of the entire density field at this time is shown in Figure 7. The two shock waves are readily apparent along with the slower Rossby waves. There is also a residual density collar surrounding at the initial vortex radius. Space-time features of these waves are further analyzed into component azimuthal modes.

(b) Averaged Flow Variables

A finite Fourier series representation is used to define azimuthal averages. For example, the mean surface density ($m = 0$ mode) and fundamental ($m = 1$ mode) are:

$$\sigma_0(r, t) = \frac{1}{N} \sum_{j=1}^N [\sigma(r, t, \theta_j) - \sigma(r, t = 0)]$$

$$\sigma_1(r, t) = \frac{1}{N} \sum_{j=1}^N \sigma(r, t, \theta_j) e^{i\theta_j}$$

where N is the number of azimuthal grid points and $\theta_j = 2\pi(j-1)/N$. Nonlinear evolution of the $m = 0$ mode is the main pathway for radial transmission of information while the $m=1$ mode with a $\cos \theta$ dependence is useful for characterizing the slower Rossby wave component. The axisymmetric perturbations of surface density and entropy characterize the wave field. The quantities $\sigma_0(r, t)$ and $s_0(r, t)$ are shown in Figures 8 and 9 at selected times to 100 yrs. These waves characterize the fastest signals emitted by the deforming vortex. The time scale for information transfer is directly related to the sound speed; it takes about 12 revolutions of the vortex at 4 AU to affect the region out to 20 AU.

The surface density in Figure 8 evolves from essentially no disturbance to a propagating density wave in about 10 yr. The evolving wave consists of a precursor compression/expansion followed by two sharp compressions and a decaying wave packet. The precursor wave decay is probably governed by geometrical spreading in the cylindrical disk. The compressions evolve into shock waves that maintain their amplitude. The stronger shock separates a weak leading shock and the trailing wave packet. This discrete wave system is the only long-range signal emitted by the continuously decaying vortex. A persistent nonlinear density remnant remains at 4 AU. Differences between rapid compressions and shock waves are not easily discernable from density profiles, but entropy changes are sensitive indicators. Figure 9 clearly shows the formation, growth, and decay of the shock waves as measured by the entropy. The first jump appears after 20 yr. at 6 AU, grows to 60 yr., and then begins to decay. Meanwhile the second stronger shock forms behind the first and feeds on its predecessor. The entropy signal is slightly contaminated by a numerical artifact from the finite difference equations but does not affect the physical nature of the evolving flow. The leading shock move at a speed ranging from .14 AU/yr at 38.4 yrs to .10 AU/yr at 96 yrs, both values being greater than the local mean sound speed. The two shock waves at 96 yrs possess temperature jumps of .003 and .873 deg K respectively, a fraction of the ambient temperature of approximately 12 deg K. Also note steadily falling entropy in the region of 4-6 AU. This is where the slower Rossby waves appear and an azimuthal average smears out the discrete nature of these disturbances.

The slower moving Rossby waves are most visible in the potential vorticity, the compressible counterpart of the conserved vorticity. Figure 10 shows a space-time graph of the fundamental ($m = 1$) component of this quantity. The shock wave positions are clearly marked along with a variable wavelength disturbance that lags the faster moving acoustically generated waves. The slow waves decay rapidly and are similar in nature to the Rossby waves in DSC.

The computed wave systems are summarized in Figure 11 against a background of characteristic curves belonging to the undisturbed flow. The family of dotted characteristics correspond to the trajectories $dr/dt = a(r) = \text{const}$ with their slopes proportional to the inverse sound speed. The two solid lines estimate the shock wave path obtained by fitting a parabola to the density peaks at

each indicated time. The shock speed decreases due to a combination of its propagating into an inhomogeneous medium and nonlinear wave interactions. Their slope is always less than the sound speed indicating a mild local supersonic shock speed. At larger radii the mean vorticity rapidly decays and acoustically generated waves should be indistinguishable from classical cylindrical weak shock waves. Considered as an inverse signaling problem, the nature of the source (as a vortex) cannot be reconstructed from this far field generic signal. The dashed lines in the figure trace maxima of the fundamental mode potential vorticity (a representative trace from Figure 10 is redrawn for clarity showing the location of both waves). Their slope is always greater than that of the background characteristics indicating a much slower phase speed. These waves remain in the vicinity of the source disturbance about twice as long as the shocks, but represent a weaker wave system.

Conclusions

Adams and Watkins 1995 present a comprehensive and still relevant overview of the many open issues related to vortices in protoplanetary disks. Here we address a few of the issues using a numerical model of the nonlinear evolution of vortices in disks. The main findings relate to bifurcation of the vortex structure into propagating wave packets and into an axisymmetric ring structure. In particular the potential vorticity (e.g. vorticity per unit surface mass) emerges as a useful structure in its own right.

The main conclusions from this investigation are: (1) As a result of Keplerian shearing motion a vortex persists for about 10 revolutions. Whether or not this is sufficient time for a critical mass of particles to accumulate needs further investigation. Even though vortex persistence is dependent on a number of parameters, it is unlikely that vortices of this size could last more than decades of orbits. However, it is clear that anticyclonic vortices are definitely more robust.

(2) Another outcome of this investigation is the non-participation of the vortex in the baseline structure of the disk. Consistent with classical notions regarding wave propagation in non participating media, the wave moves through the disk without materially affecting it. Global mass accretion and angular momentum transfer in protostellar disks are associated with large-scale, widely-spaced asymmetrical spirals of matter while the wave packets computed here are restricted to tightly-wound spirals and axisymmetric shocks.

(3) The response of disks with other equilibrium profiles may be quite different. If self-gravitating effects are included (heavy disks, e.g. Laughlin et al 1998) vortex-induced instabilities could "light up" the disk with strong transient signals and drive accretion and angular momentum transfer processes via gravitational torques. Another possibility is that thermal instabilities due to thickness gradients or radial entropy gradients could induce significant transient events. In any event it is hard to see how any of these time-limited effects could sustain global turbulence in the disk and be active for long epochs. The only possibility would be an almost continuous barrage of external vortex-inducing events.

Acknowledgments

The author would like to thank M. M. Rai for access to his source codes and helpful suggestions, to Greg Laughlin and Jeff Cuzzi for stimulating discussions on disk dynamics, and to the Ames Directors Discretionary Fund for supporting this effort.

References

- Adams, F. C., Ruden, S. P., & Shu, F. H. 1989, *ApJ*, 347, 959
 Adams, F.C. & Watkins, R. 1995, *ApJ*, 451, 314
 Barge, P. & Sommeria, J. 1995 *A&A*, 295, L1
 Boss, A. 1993, *ApJ*, 417, 351
 Bracco, A., Chavanis, P. H., & Provenzale, A. 1999, *Phys. Fluids*, 11, 2280
 Bracco, A., Provenzale, A., Speigel, E. A., & Yecko, P. 1998, in *Theory of Black Hole Accretion Disks*, eds. M. Abramowicz et al., (Cambridge: Cambridge U. Press)
 Cuzzi, J., Dobrovolskis, T., & Champney, J. 1993, *Icarus*, 106, 102
 Davis, S. 2001a, *ApJS* (submitted)
 Davis, S., Sheehan, D., & Cuzzi, J. 2000, *ApJ*, 545, 494
 Godon, P. & Livio, M. 1999, *ApJ.*, 523, 350
 Godon, P. 1997, *ApJ*, 480, 329
 Hunter, C. 1972, "Self Gravitating Gaseous Disks," in *Annu. Rev. Fluid Mechanics* 219
 Klahr, H., Henning, Th., & Kley, W. 1999, *ApJ*, 514, 315
 Li, H., Colgate, S. A., Wendroff, B., & Liska, R. 2001, *ApJ*, 551, 874
 Laughlin, G., Korchagin, V., & Adams, F. C. 1998, *ApJ*, 504, 945
 Lebovitz, N. R. 1979, in *Annu. Rev. Fluid Mechanics*, eds. M. Van Dyke et al. (Palo Alto: Annual Reviews Inc.), 229-246.
 Li, H., Finn, J. M., Lovelace, R. V. E., & Colgate, S. A. 2000, *ApJ*, 533, 1023
 Lovelace, R. V. E., Li, H., Colgate, S. A., & Nelson, A. F. 1999, *ApJ*, 513, 805
 Lowrie, R. B., Morel, J. E., and Hittinger, J. A., 1999 *ApJ* 521, 432.
 Lynden-Bell & Pringle, 1974, *MNRAS*, 168, 603
 Mair, G., Muller, E., Hillebrandt, W., and Arnold, C. N. 1988, *A&A*, 199,114
 Papaloizou, J. & Lin, D. N. C. 1995, in *Annu. Rev. Astron. Astrophys.*, (Palo Alto: Annual Reviews Inc.), 505
 Ruden, S., Papaloizou, J. C. B., and Lin D. N. C.,1988, *ApJ*, 329, 739.
 Sheehan, D., Davis, S., Cuzzi, J., & Estberg, G. 1999, *Icarus* 142, 238
 v. Weizsacker, C. F. 1944, *Z. fur Astrophys.*, 22, 319
 Weidenschilling, S. J. and Cuzzi, J. N., *Protostars & Planets III*, 1993, 1031
 Weidenschilling, S. J., 1977, *MNRS*, 180, 57.

Appendix Mechanical Equilibrium

A polytropic gas rotates only under the influence of a central gravitator. An approximate equilibrium solution is presented in Ruden et al. 1988 and Boss 1993. Here we will describe the mechanical equilibrium as a general solution of the governing partial differential equation. In spherical coordinates the three non-vanishing flow quantities are the rotational velocity V_ϕ , the density ρ and the pressure p . All three are independent of the azimuthal coordinated ϕ . The system is closed by a polytropic equation of state $p(R,\theta) = K \rho(R,\theta)^\gamma$ where K is the polytropic constant and γ is the ratio of specific heats. If the pressure is eliminated, the two remaining equations that conserve rotational and radial momentum are:

$$\begin{aligned} -\rho V_\phi^2 \cot \theta + K \gamma \rho^{\gamma-1} \frac{\partial \rho}{\partial \theta} &= 0 \\ -\rho \frac{V_\phi^2}{R} + K \gamma \rho^{\gamma-1} \frac{\partial \rho}{\partial R} + \frac{GM\rho}{R^2} &= 0 \end{aligned} \quad (A1)$$

Eliminate the rotational velocity to obtain a first order partial differential equation for the quantity $\rho^{\gamma-1}$:

$$R^2 \cos \theta \frac{\partial \rho^{\gamma-1}}{\partial R} + \frac{\gamma-1}{K\gamma} GM \cos \theta - R \sin \theta \frac{\partial \rho^{\gamma-1}}{\partial \theta} = 0 \quad (A2)$$

The general solution of this partial differential equation for $\rho^{\gamma-1}$ involves an arbitrary function of the quantity $R \sin \theta$ that is just r , the radial distance from the axis of rotation.

$$\rho^{\gamma-1} = f(R \sin \theta) \left[1 - \frac{\gamma-1}{K\gamma} \frac{GM}{f(R \sin \theta)} \left(\frac{1}{R \sin \theta} - \frac{1}{R} \right) \right] \quad (A3)$$

Identify $f(r)$ with the $(\gamma-1)$ st-power of the arbitrary central-plane density $\rho_c(r)$ to complete the solution. The pressure is easily obtained from the polytropic law and the azimuthal velocity from the first of eq (A1). The final relation among the three quantities are:

$$\begin{aligned} \rho(R,\theta) &= \rho_c(r) \left[1 - \frac{\gamma-1}{\gamma} \frac{GM}{a_c^2} \left(\frac{1}{R \sin \theta} - \frac{1}{R} \right) \right]^{1/(\gamma-1)} \\ p(R,\theta) &= p_c(r) \left[1 - \frac{\gamma-1}{\gamma} \frac{GM}{a_c^2} \left(\frac{1}{R \sin \theta} - \frac{1}{R} \right) \right]^{\gamma/(\gamma-1)} \\ V_\phi^2(R,\theta) &= \frac{GM}{R \sin \theta} \left[1 + \frac{\gamma a_c^2}{GM} R \sin \theta \frac{d \log \rho_c}{d \log r} \right] \end{aligned} \quad (A4)$$

where a_{ci} is the isothermal sound speed defined by the square root of p_c/ρ_c . A reasonable approximation to eq (A4) in cylindrical coordinates is to let $R \sim r$ and expand $1/r-1/R$ in a Taylor series about $z = 0$. The final mechanical equilibrium state for a thin disk is:

$$\begin{aligned} \rho &= \rho_c(r) \left[1 - \frac{\gamma-1}{2\gamma} \frac{GM}{a_{ci}^2} \frac{z^2}{r^2} \right]^{1/(\gamma-1)} \\ p &= p_c(r) \left[1 - \frac{\gamma-1}{2\gamma} \frac{GM}{a_{ci}^2} \frac{z^2}{r^2} \right]^{\gamma/(\gamma-1)} \\ V_\phi^2 &= \frac{GM}{r} \left[1 + \frac{\gamma a_{ci}^2}{GM} r \frac{d \log \rho_c}{d \log r} \right] \end{aligned} \quad (A5)$$

The coefficient of the term multiplying z^2/r^2 proportional to the ratio of the local gravitational potential energy GM/r to the thermal energy squared. For a typical protoplanetary nebula this ratio is $O(10^3)$ so the thermodynamic quantities decrease very rapidly from $z = 0$. The azimuthal velocity, on the other hand, depends only on the radius r and is independent of z , which is a general statement for a barotropic fluid (Lebovitz 1979, p 236). The density and pressure decay rapidly from the midplane while the rotational velocity remains very close to the Keplerian value throughout the flow field. (The coefficient of the corresponding term in V_ϕ is now the inverse of the energy ratio mentioned above.) These formulas are the same as those used by other investigators concerned with vertical equilibrium in polytropic disks.

The "column-averaged" density (σ) and pressure (P) are obtained by integrating the quantities over a disk whose half-height H is the inverse of the coefficient of z^2 in the above formulas. The equations for the surface density and surface pressure are (Hunter, 1972, p 224):

$$\begin{aligned} \sigma &= \rho_c(r) \int_{-H}^H \left[1 - \frac{z^2}{H^2} \right]^{1/(\gamma-1)} dz = H \rho_c(r) \int_{-1}^1 [1-x^2]^{1/(\gamma-1)} dx = \alpha H \rho_c(r) \\ P &= p_c(r) \int_{-H}^H \left[1 - \frac{z^2}{H^2} \right]^{\gamma/(\gamma-1)} dz = H p_c(r) \int_{-1}^1 [1-x^2]^{\gamma/(\gamma-1)} dx = \beta H p_c(r) \end{aligned} \quad (A6)$$

where α and β are defined by Gamma functions that depend only on the ratio of specific heats γ .

Now let the variation of the central density and pressure be simple power laws of the radial coordinate; $\rho_c(r) = \rho_0 (r/r_0)^m$ and $p_c(r) = p_0 (r/r_0)^n$. It follows that the variation of H obeys the power law $H(r) = H_0 (r/r_0)^\mu$ where $H_0 = (2\gamma p_0/\rho_0 / (\gamma-1)/GM)^{1/2}$ and $\mu = (3-m+n)/2$. The surface density and pressure now have spatial variations of the form $\sigma(r) = \alpha \rho_0 H_0 (r/r_0)^{m+\mu}$ and $P(r) = \beta p_0 H_0 (r/r_0)^{n+\mu}$. This is a parametric representation relating surface density and pressure in terms of r . Eliminating r implies the relation between σ and P :

$$P = \frac{\beta H_0}{(\alpha H_0)^{\frac{n+\mu}{m+\mu}}} \sigma^{\frac{n+\mu}{m+\mu}} = K' \sigma^\Gamma$$

which indicates that the surface thermodynamic quantities are also polytropes with a modified K and a different specific heat ratio. The exponents m and n are constrained so that $m\gamma - n = 0$.

In summary, mechanical equilibrium is defined by the given quantities ρ_0 , p_0 , r_0 , n , GM , and γ . The derived quantities are m , α , β , μ , Γ , and H_0 . Table AI shows representative values of those parameters in terms of γ for the case when $n = -3$.

TABLE AI
Values of the Equilibrium Parameters ($n = -3$)

γ	m	α	β	μ	Γ
1.2	-2.500	0.739	0.682	1.250	1.4
1.3	-2.308	0.876	0.786	1.154	1.6
1.4	-2.143	0.982	0.859	1.071	1.8
1.5	-2.000	1.067	0.914	1.000	2
1.6	-1.875	1.137	0.958	0.938	2.2

List of Figures

1. Vortex location and induced velocity field at initial instant of time. The vortex is located at about 135 deg on the $r = 4$ AU circle.
2. Contours of equal strength vorticity relative to minimum (maximum) vorticity at each time step. Time is measured by vortex revolutions at 4 AU. (a) Initial cyclonic vortex, perturbation vorticity > 0 . (a) Initial anticyclonic vortex, perturbation vorticity < 0 .
3. Vorticity profile along a ray at 163 deg showing decay of initial vorticity at 4 AU and instantaneous location of the wave field. Shock waves have already formed in the region 6-8 AU.
4. Contours of (a) vorticity in an incompressible disk model, (b) potential vorticity in a compressible disk model. Anticyclonic vorticity shown using the same scale as Figure 2.
5. Contours of (a) vorticity and (b) surface density after 1.37 revolutions of the initial vortex. Rapid shearing and initial wave systems are apparent.
6. Evolution of the surface density over the entire simulated disk, $1 < r, \text{ AU} < 24$. (a) Initial flow, (b) 4 revs, (c) 8 revs, (d) 12 revs.
7. Perspective view of the total surface density at 12 revs. (Note: perturbed density drawn to twice the scale of the equilibrium density for clarity.)
8. Profiles of mean perturbation surface density $\sigma_0(r, t)$ at selected times showing global shock wave propagation in the disk.
9. Values of mean perturbation entropy $s_0(r, t)$ indicating discontinuities at the shock wave position.
10. Potential vorticity profiles for the $m = 1$ mode showing $\cos \theta$ dependence of slower moving Rossby waves.
11. Space-time diagram of shock wave trajectories (solid), Rossby wave tracks (dashed), and equilibrium flow characteristic curves (dotted).

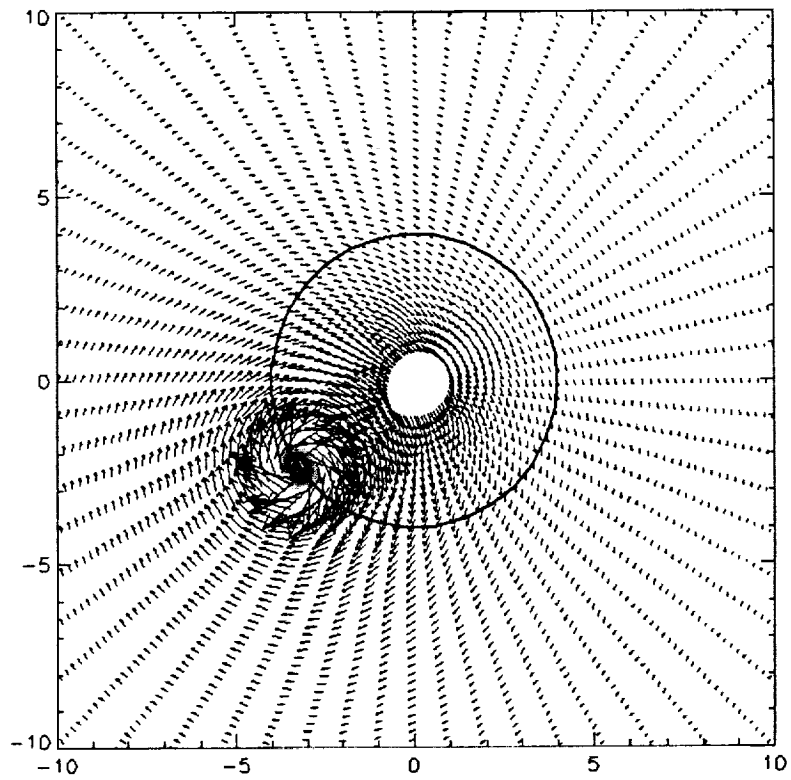


Figure 1

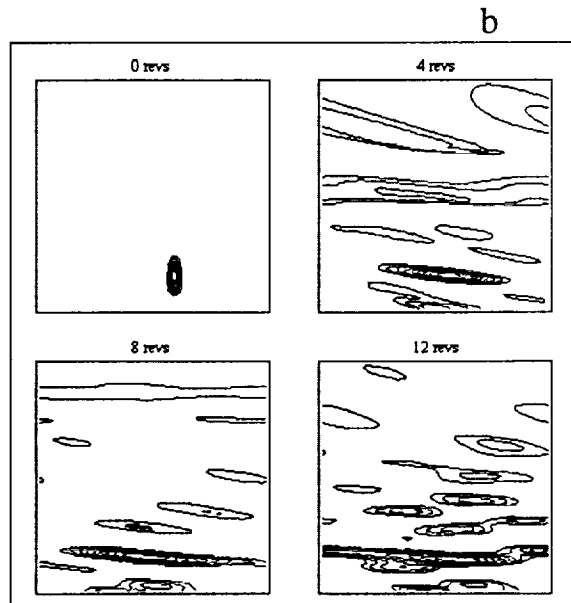
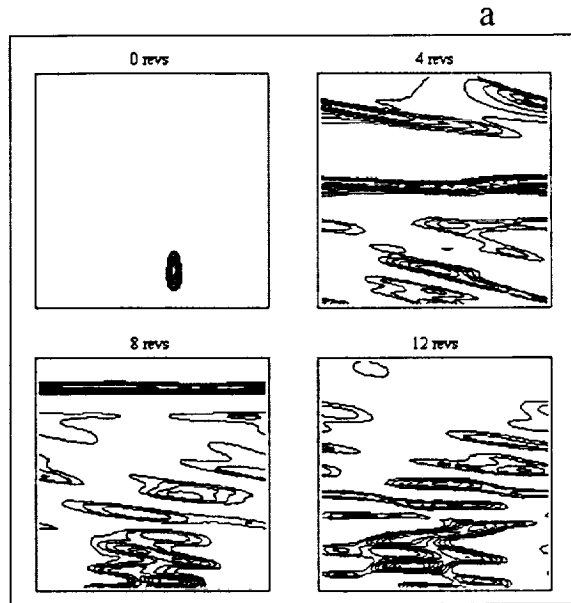


Figure 2

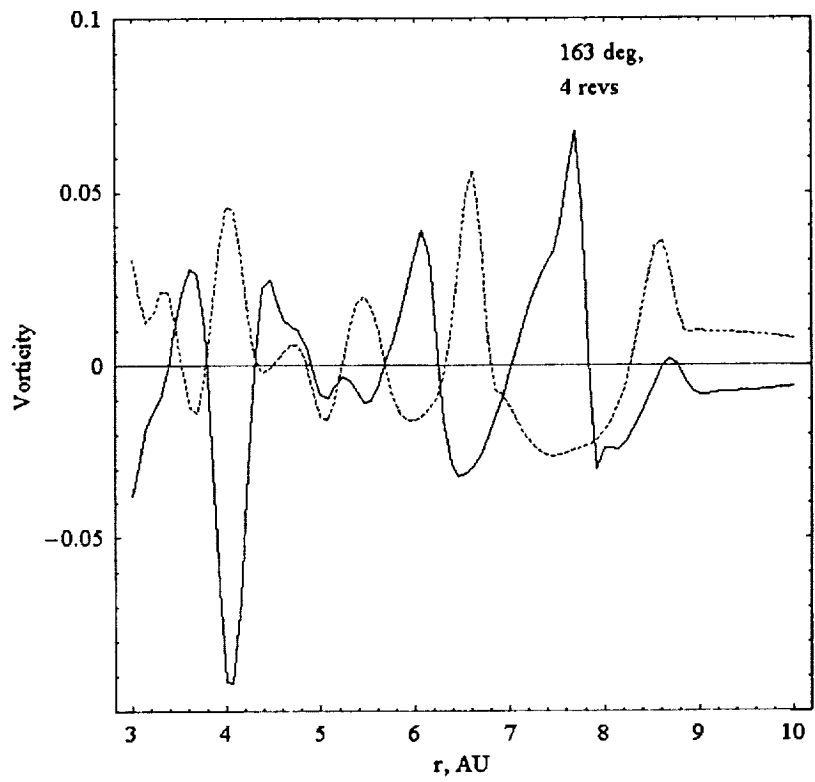
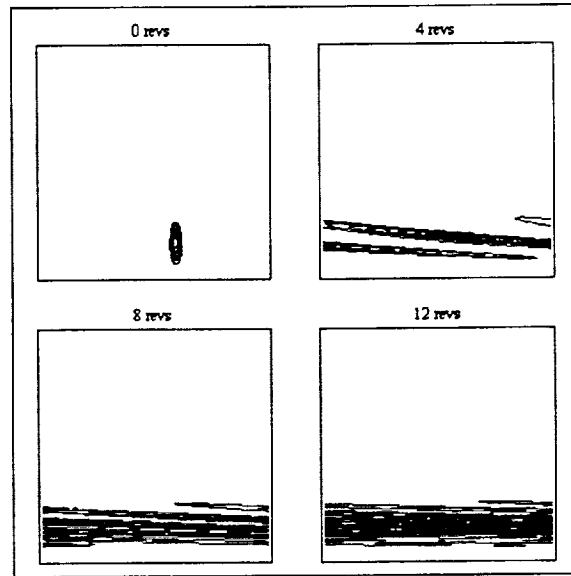


Figure 3

a



b

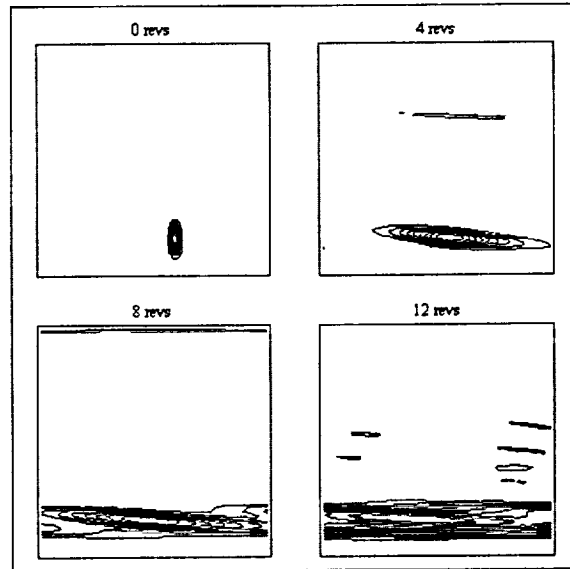


Figure 4

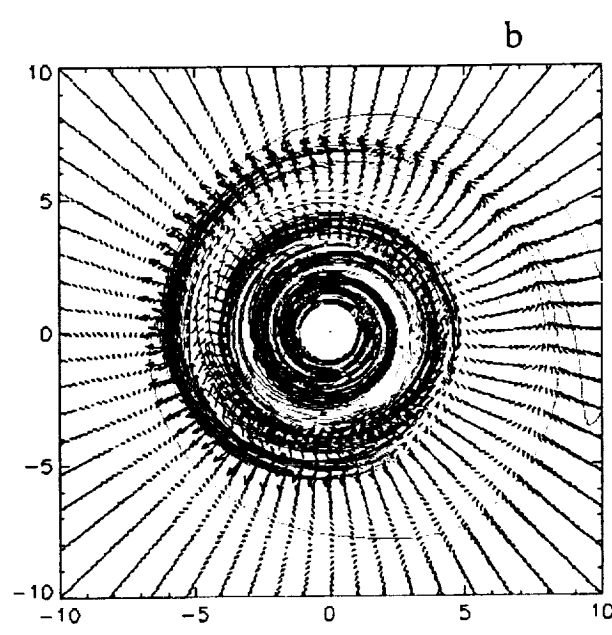
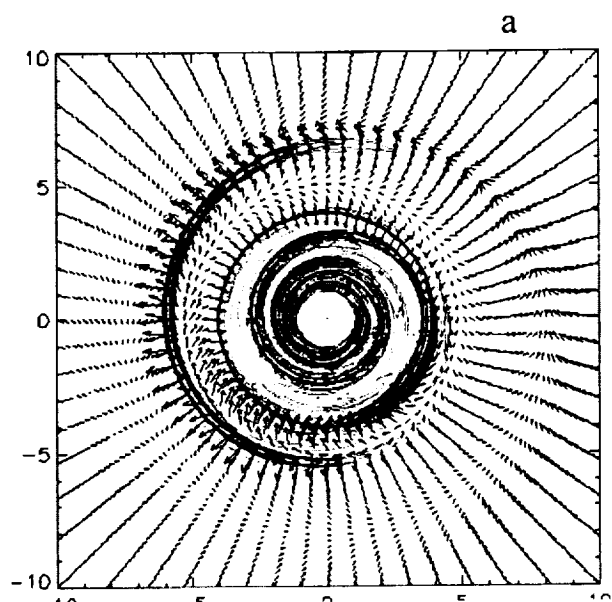


Figure 5

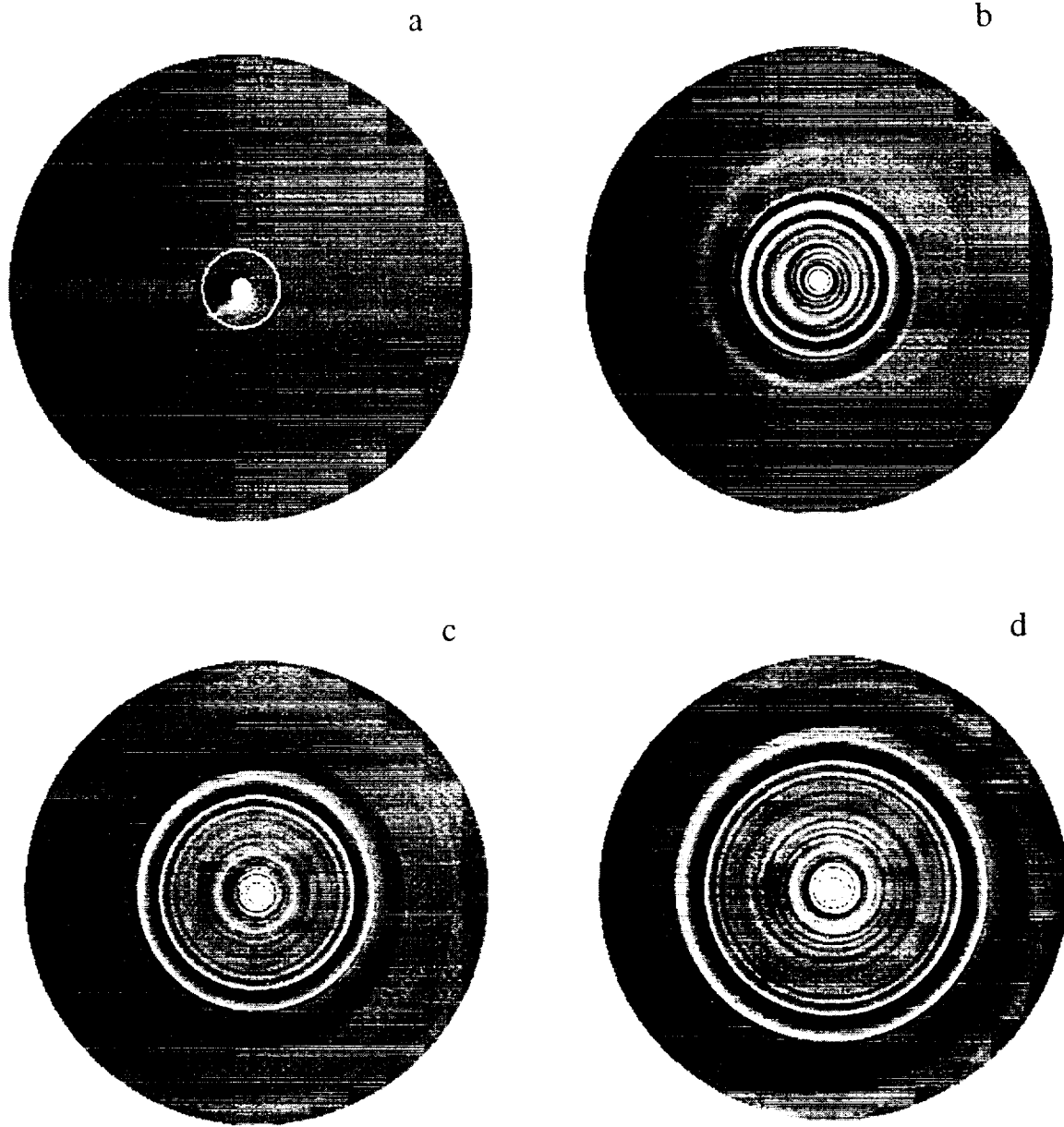


Figure 6

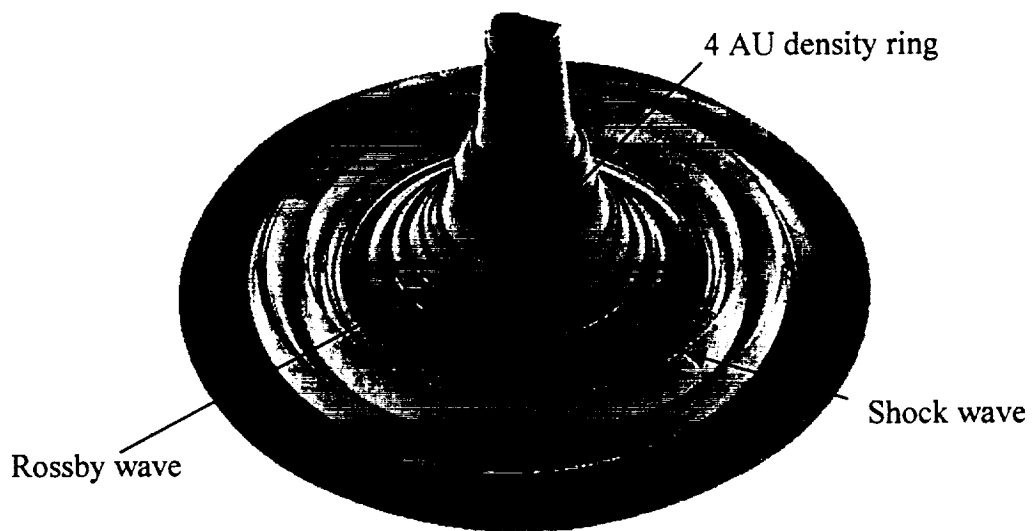


Figure 7

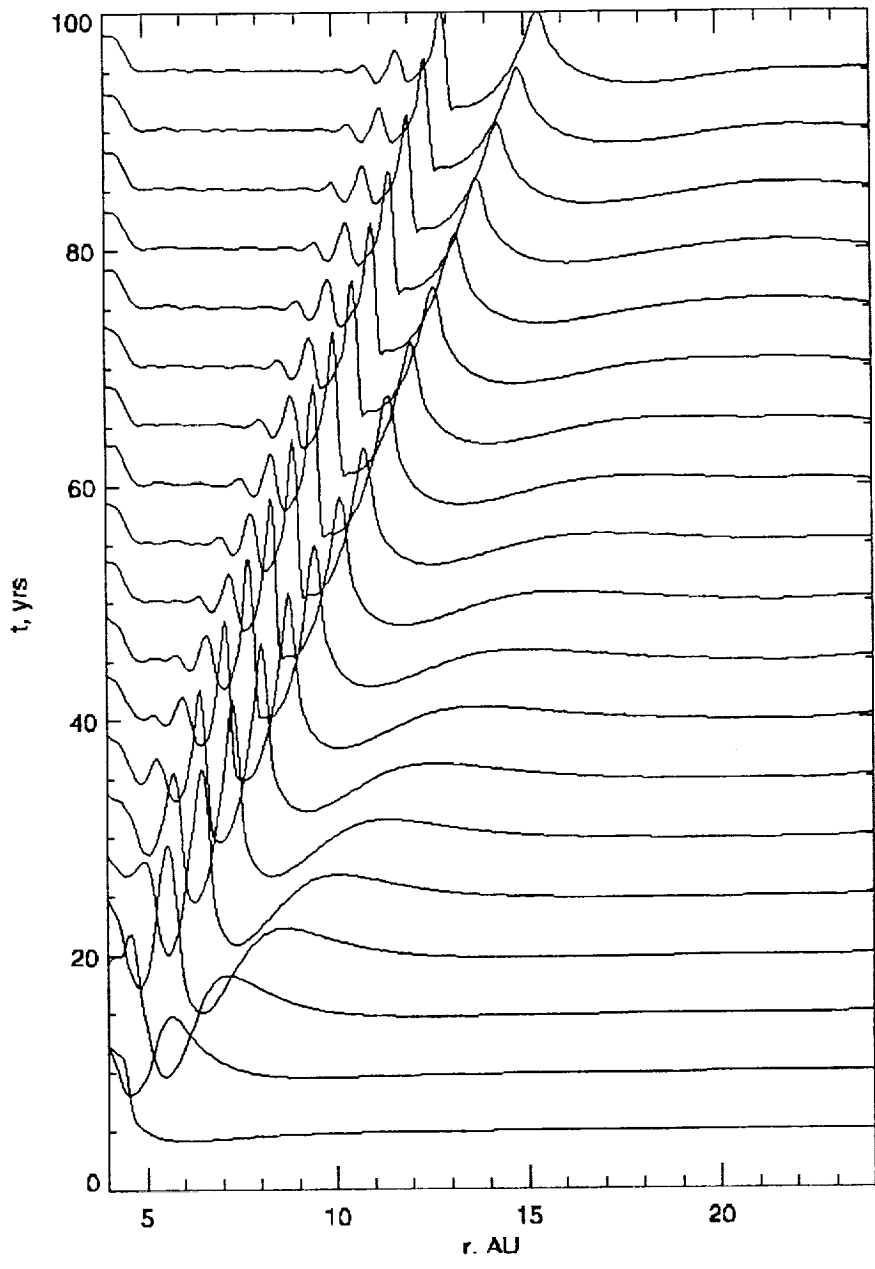


Figure 8

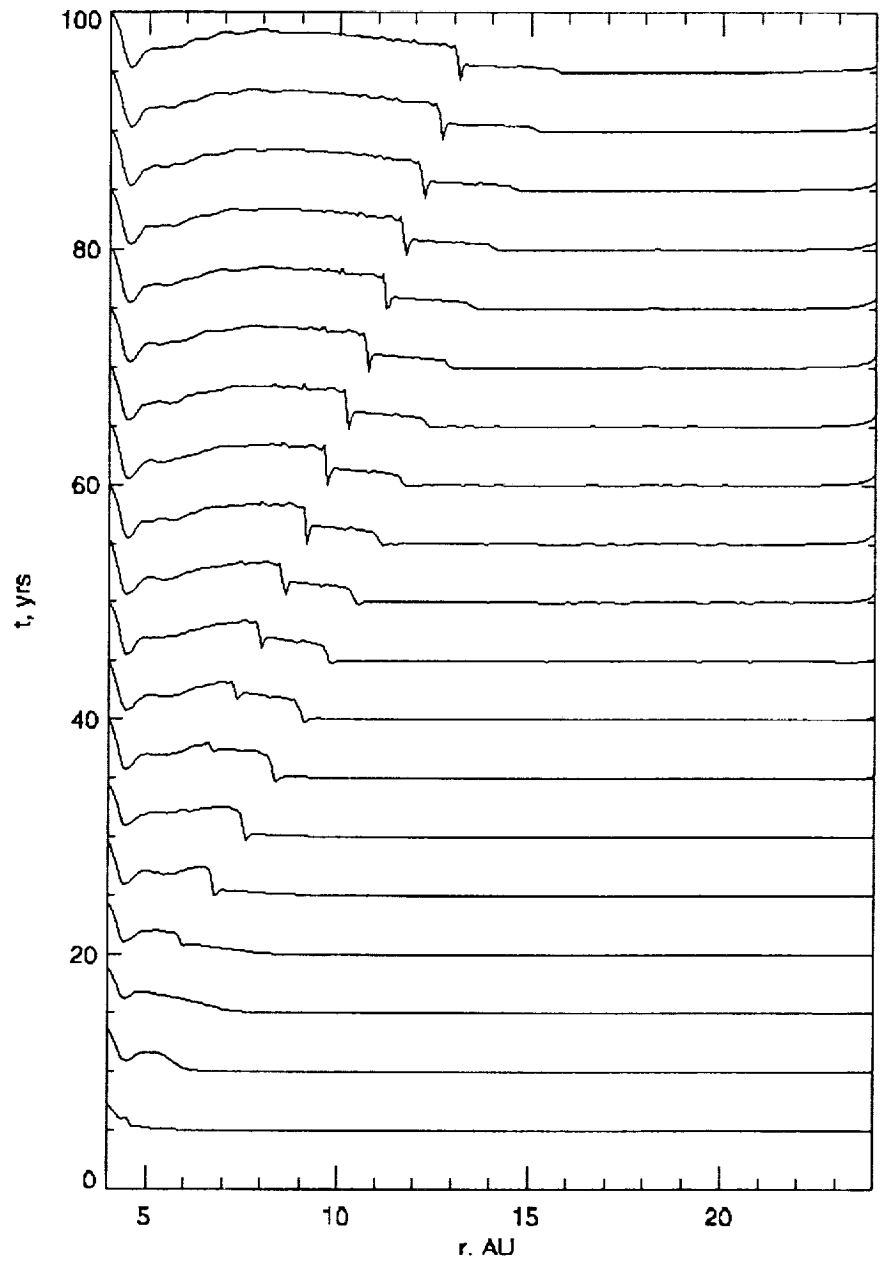


Figure 9

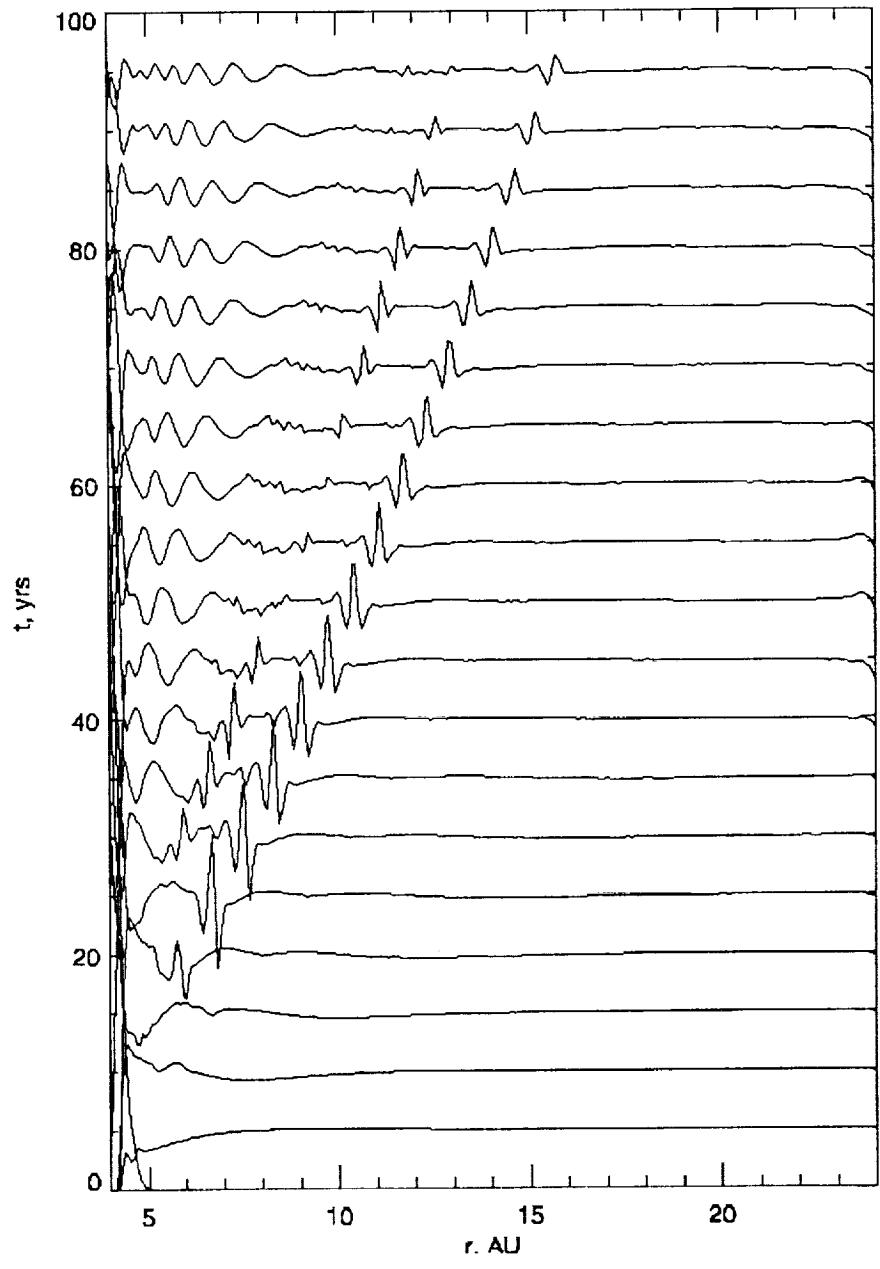


Figure 10

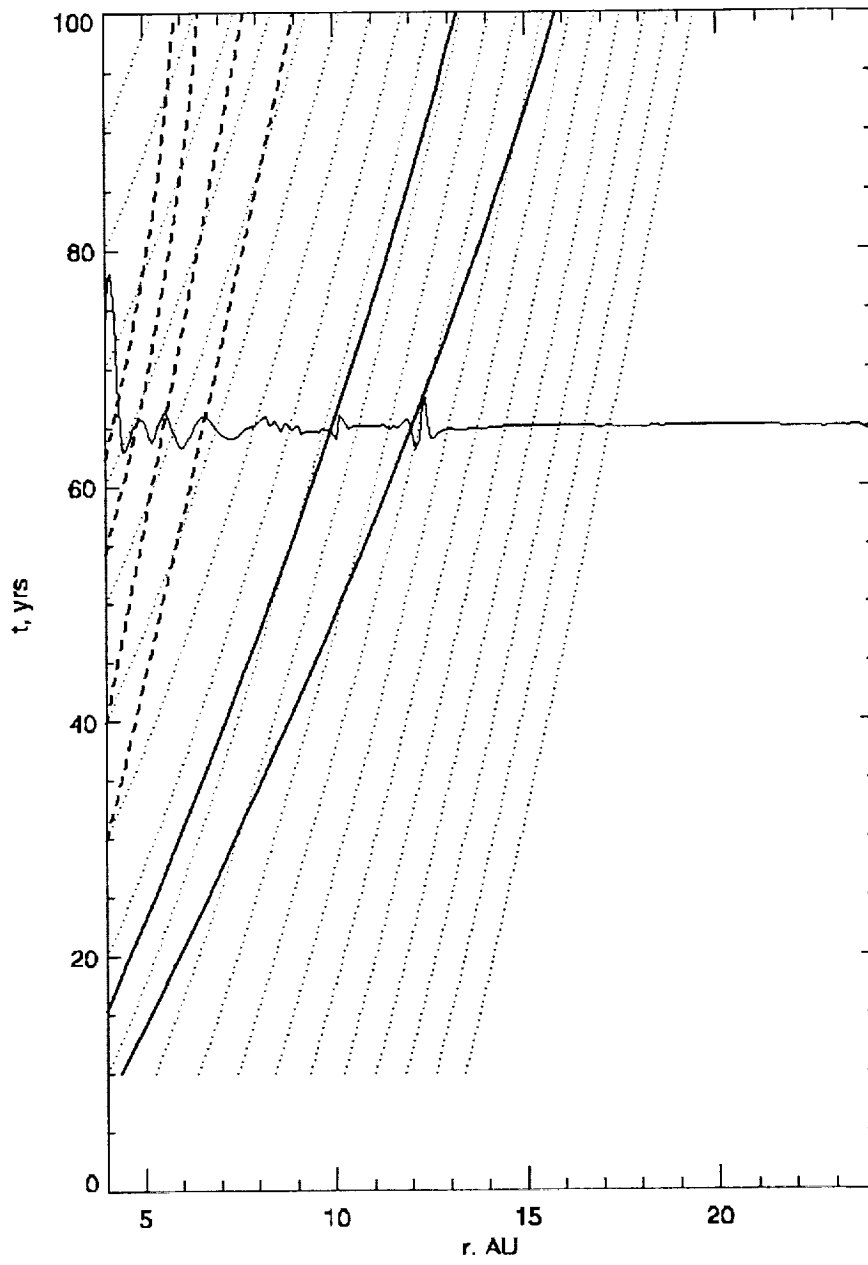


Figure 11